Cryogenic irradiation of an EMCCD for the WFIRST coronagraph: preliminary performance analysis

Conference or Workshop Item

Cryogenic Irradiation of an EMCCD for the WFIRST Coronagraph: Preliminary Performance Analysis

Nathan Bush[a] *, David Hall[a], Andrew Holland[a], Ross Burgon[a], Neil Murray[a], Jason Gow[a], Douglas Jordan[b], Richard Demers[c], Leon K. Harding[c], Bijan Nemati[c], Michael Hoenk[c], Darren Michaels[c], and Pavani Peddada[c]

[a] Centre for Electronic Imaging, The Open University, Walton Hall, Milton Keynes, MK7 6AA, UK

[b] e2v Technologies plc, Waterhouse Lane, Chelmsford, Essex CM1 2QU, UK

[c] Jet Propulsion Laboratory, California Institute of Technology, 4800 Oak Grove Drive, Pasadena, California, 91109, United States

ABSTRACT

The Wide Field Infra-Red Survey Telescope (WFIRST) is a NASA observatory scheduled to launch in the next decade that will settle essential questions in exoplanet science. The Wide Field Instrument (WFI) offers Hubble quality imaging over a 0.28 square degree field of view and will gather NIR statistical data on exoplanets through gravitational microlensing. An on-board coronagraph will for the first time perform direct imaging and spectroscopic analysis of exoplanets with properties analogous to those within our own solar system, including cold Jupiters, mini Neptunes and potentially super Earths.

The Coronagraph Instrument (CGI) will be required to operate with low signal flux for long integration times, demanding all noise sources are kept to a minimum. The Electron Multiplication (EM)-CCD has been baselined for both the imaging and spectrograph cameras due its ability to operate with sub-electron effective read noise values with appropriate multiplication gain setting. The presence of other noise sources, however, such as thermal dark signal and Clock Induced Charge (CIC), need to be characterized and mitigated. In addition, operation within a space environment will subject the device to radiation damage that will degrade the Charge Transfer Efficiency (CTE) of the device throughout the mission lifetime. Irradiation at the nominal instrument operating temperature has the potential to provide the best estimate of performance degradation that will be experienced in-flight, since the final population of silicon defects has been shown to be dependent upon the temperature at which the sensor is irradiated.

Here we present initial findings from pre- and post- cryogenic irradiation testing of the e2v CCD201-20 BI EMCCD sensor, baselined for the WFIRST coronagraph instrument. The motivation for irradiation at cryogenic temperatures is discussed with reference to previous investigations of a similar nature. The results are presented in context with those from a previous room temperature irradiation investigation that was performed on a CCD201-20 operated under the same conditions. A key conclusion is that the measured performance degradation for a given proton fluence is seen to measurably differ for the cryogenic case compared to the room temperature equivalent for the conditions of this study.

Keywords: WFIRST, CGI, coronagraph, EMCCD, CCD, radiation damage, cryogenic irradiation, silicon defects, annealing, displacement damage

*Corresponding author.
Email: nathan.bush@open.ac.uk

1. THE WFIRST CORONAGRAPH

The Wide Field Infrared Survey Telescope (WFIRST) is a NASA observatory scheduled to launch in the next decade with two complementary scientific payloads. The Wide-Field Imager (WFI) will perform large-scale surveys of the NIR sky and gather statistical data of exoplanets planets through gravitational micro-lensing events. The Coronagraph Instrument (CGI) will perform highly detailed characterisation of a sample of exoplanets and debris disks through both photometric and spectroscopic observations. The coronagraph can operate in two modes, a hybrid Lyot coronagraph for photometry and a shaped pupil coronagraph for exoplanet spectroscopy and debris disk characterisation. The CGI is capable of switching between the two modes through rotary mechanisms that change appropriate masks and filters. A fold mirror directs the optical beam to one of two camera systems, the imaging camera is selected for photometry whereas the Integral Field Spectrometer (IFS) is used for spectrometry.

A key objective of the coronagraph is to directly image giant planets in the range of the habitable zones to beyond the ice lines, for the first time directly imaging planets similar to those within our own Solar System.[1] Observing such candidates requires the capability to sustain high contrast within a small inner working angle. Each aspect of the coronagraph has been engineered with the science requirements in mind, with more detail concerning the design and operation of the instrument discussed within Noecker et al. (2016),[2] Harding et al. (2015)[3] and the references therein. The result is an instrument which represents a significant advancement within the field of high contrast imaging in space and has advanced the TRL of technologies that will be required for future missions with similar ambitious science objectives.

The apparent brightness of candidate objects and combined processes for starlight suppression result in an extremely small expected signal flux for each camera system. Each detector will be required to routinely detect signals at the single photon level throughout the nominal 6-year mission duration. The requirement for sub-electron detector noise has positioned the CCD201-20,[4] a commercially available EMCCD from e2v technologies, as the baseline detector for both the CGI imaging camera and IFS.[3]

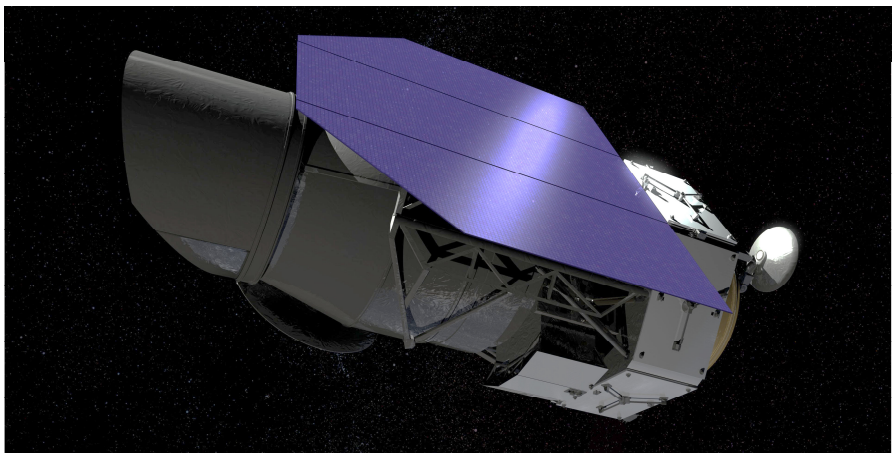

Figure 1: WFIRST mission concept.[1]

2. EMCCD TECHNOLOGY

The ultimate limit of CCD sensitivity is due the noise introduced by the output amplifier, which can be reduced to 2-3 e^- at suitably slow scan rates.[5] Signal levels for both CGI camera systems are rarely expected to rise above the single photon level and so a detector that can achieve sub electron read noise is predicted to provide a substantial benefit to the net scientific performance of the instrument.[1] The Electron Multiplication CCD (EMCCD) is a variant of traditional CCD technology that can achieve the required sub-electron effective read noise values and so is well suited to applications such as the CGI that demand high speed operation under photon starved conditions.[5] An image area, readout register and output amplifier are all present that are of conventional design (Figure 2). The feature unique to this technology is an electron multiplication register, appended to the standard readout register, that amplifies signals within the charge domain prior to voltage conversion at the output node.

In practise this is achieved through a 4-gate structure with two gates customised to generate a region of high electric field. The ϕDC gate is constantly biased to between 3-5 V and acts a potential barrier to prevent the motion of charge while the high field is established. The Rϕ2HV phase has a timed, high-voltage pulse applied that accelerates the signal carriers to energies sufficient for the generation of additional electron-hole pairs through the process of impact ionisation. The remaining two electrodes (ϕ1, ϕ3) operate at standard potentials and act to transfer charge from one multiplication element to the next. Appropriate clocking of the gates allows the signal to be transferred from the previous element, experience multiplication, and be passed to the following element where the process repeats (Figure 2). The amplification per element is typically small (1-1.5%), however, the consecutive operation of multiple elements (typically 500) allows high multiplication gain factors with operating voltages for the Rϕ2HV gate in the range of 35-45 V.

The multiplication process amplifies signals such that it becomes appropriate to designate an *effective* read noise to the system; defined as the baseline read noise divided by the applied multiplication gain. Multiplication gain values in the range of a few hundred can therefore reduce the read noise to sub-electron levels. Under these conditions the noise limitation of the output amplifier is effectively eliminated, allowing the device to operate at MHz pixel rates while maintaining the ability to image down to the single photon level. This feature allows the device to surpass the noise performance of standard CCD technology under operating conditions where the read noise is comparable to the signal level of interest.[6]

The multiplication process is stochastic and so introduces an additional noise component, quantified as a factor increase in Poisson noise (for optical photons) and termed the Excess Noise Factor (ENF). The ENF has been shown to tend to $\sqrt{2}$ for a large number of multiplication elements operating at high gain.[6] For sufficiently low optical signal levels ($\leq$ 20 e$-$/pix/s) some reduction in the ENF is possible through post-processing techniques.[7] Operation in "binary mode", where the output of each pixel is assessed against a fixed threshold (commonly 5σ above the total noise floor) can reduce the ENF to unity, thereby permitting the detection of single photons. For the CGI application, operation in either analogue gain mode (with the ENF) or photon counting mode translates into a significantly reduced total integration time for a given exoplanet target when compared to the use of a standard scientific CCD counterpart.[3]

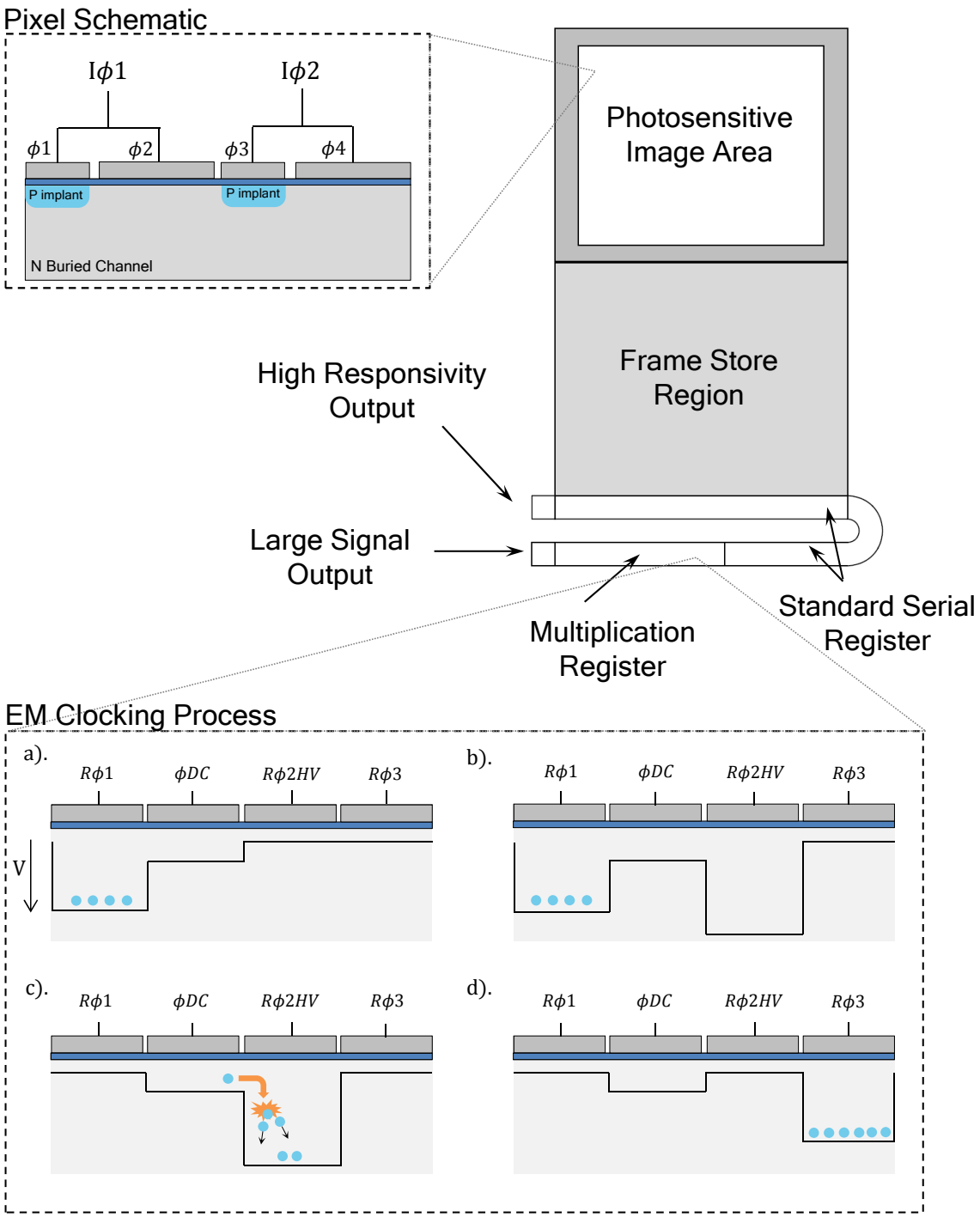

Figure 2: Example EMCCD schematic, adapted from the CCD201-20 datasheet.[4] The image pixel schematic is shown perpendicular to the direction of transfer for clarity. Also shown is an example EMCCD clocking sequence. (b) The ϕDC phase prevents the motion of charge while the high field is established. (c) Carriers are accelerated to energies sufficient for impact ionisation as the charge is transferred between ϕDC and Rϕ2HV. (d) The signal can then be transferred to the following multiplication element where the process repeats.

3. EMCCDS FOR THE WFIRST CGI

The EMCCD baselined for each of the CGI camera systems is the CCD201-20; a 1k×1k frame transfer device that offers the capability to run as either a standard scientific CCD through the HR output or as an EMCCD through the LS output (Figure 2).[4] The image and store sections of the device nominally operate in 2-phase inverted mode operation (IMO) which is facilitated though the inclusion of barrier implants that deform the electronic potential to prevent the back-flow of charge during standard clocking. Operation in Non Inverted Mode (NIMO) is also possible through alterations to the operating biases of the detector.

The current CGI detector requirements specify an effective read noise value of 0.2 e^-. The exact multiplication gain necessary to meet this requirement is dependant upon the baseline read-noise of the camera electronics, which itself depends upon the chosen pixel rate. The study performed by Harding et al. (2015)[3] has shown that the baseline read noise remains below 90e^- for horizontal scan rates up to 10 MHz using the *Nüvü* EMN2 camera system. This limits the maximum required multiplication gain to ≈450, with lower gain values required for slower scan rates. Operation in photon counting mode may demand higher multiplication gain factors in order to adequately set a threshold such that photo-electron events are correctly distinguished from spurious noise. Regardless, the investigation has shown that the read noise requirement can be met with modest multiplication gain values. With the successful reduction of read noise, the dominant beginning of life (BOL) on-chip noise sources for the CGI are expected to be thermal dark signal and Clock Induced Charge (CIC).

Thermal dark signal constitutes signal carriers thermally promoted into the conduction band from bulk and/or interface states. Surface dark signal from interface traps typically dominates the bulk dark signal by at least an order of magnitude, but can be suppressed through operation in IMO whereby the interface states are flooded with holes and prevented from contributing to the background signal level. In this operating mode only the bulk dark signal remains, and has been measured in multiple studies to be lower than the nominal 5×10^{-4} e^-/pix/s requirement for the coronagraph camera systems at the baseline operating temperature.[3]

CIC is signal that is generated through the process of clocking the device. As an image phase is biased high, charge carriers at the semiconductor-insulator interface experience electric fields in excess of 10^6 Vm^{-1}, accelerating them to energies sufficient for the generation of additional carrier pairs. The additional electron can be collected within the pixel potential well and is indistinguishable from a photo-generated electron, adding noise to the system. The impact ionisation process is exponentially dependent upon the applied electric field and so CIC is strongly dependent upon the image clock high amplitude. Operation in inverted mode is also known to increase CIC by orders of magnitude since this increases the population of holes at the interface that are subject to high electric fields.

Mitigation of CIC is possible through appropriate clocking of the device such that interface states experience high electric fields for the shortest amount of time possible. As such, in some cases faster pixel rates have been linked to lower measured CIC.[8] By similar explanation, customised clocking schemes have been shown to reduce CIC significantly through limiting the maximum possible clock swing the device experiences during operation.[9] Measurements of CIC at pixel rates deemed applicable for the coronagraph camera systems have yielded values that are within the nominal requirement for the mission at the beginning of life. Further optimisation techniques are being explored at JPL that have the possibly of lowering this noise contribution further still.[3]

In summary, the BOL performance requirements for the EMCCD based coronagraph camera systems have been met by the CCD201-20 sensor.[3] The subject of more detailed study is the projected EOL performance of the detector; throughout the nominal mission lifetime the observatory will be subject to ionising and non-ionising damage that will degrade the performance of each camera system. This degradation must be characterised as accurately as possible in order to fully understand the potential impact on the coronagraph science objectives. Detailed characterisation will also aid the development of mitigation strategies that can act to recover lost performance in-flight. Such information is not only useful for the case of the WFIRST CGI, but a variety of future space missions that may image faint light sources using this technology within the coming decades.

4. RADIATION DAMAGE EFFECTS

Throughout the nominal 6-year mission radiation from both solar and galactic sources will subject the detector to ionising and non-ionising damage which physically degrades the detector and impacts performance. For the orbits under consideration for the WFIRST mission (i.e. Geosynchronous or L2)[3] the majority of damage is expected to be due to either solar protons and/or trapped protons and electrons within the radiation belts. The trapped electrons are typically low energy when compared to protons and so can be absorbed by the shielding that surrounds the focal plane as long as it is an adequate thickness or density. Trapped and solar protons, however, can have energies up to several hundred MeV and so cannot be shielded against within typical mission size and weight budgets.[10]

As an energetic proton travels through the device it loses the majority of its energy ($\geq$99%) through coulombic interactions with the lattice, generating electron-hole pairs along its trajectory though ionising damage. During operation, a proton event (included under the collective term 'cosmic ray') may therefore manifest as temporary signal since any electrons generated in the bulk may diffuse into the potential wells of one or more pixels. The effects due to ionising damage within the bulk silicon are mostly transient and do not cause permanent damage. A high number of proton events within a given frame, however, can be problematic in the sense that they can obscure the true signal under observation. Cosmic rays can therefore place a limit on the total permissible single frame integration time. An additional complication is present for EM devices whereby if a cosmic ray deposits a large amount of signal within one of more pixels it will be multiplied within the EM register and can bloom across the row. A discussion concerning one of the physical mechanisms behind this effect can be found in Bush et al. (2014), and a study concerning ground-based measurements of cosmic ray fluence for the CCD201-20 can be found in Harding et al. (2015).[3]

While the effects within the bulk are transient, ionising damage within the gate-dielectric can give rise to permanent degradation. Charge generated within the insulator layers can be less mobile than within the bulk, with holes being much less mobile in the oxide layer than electrons, for example.[11] The electron may therefore migrate away from the generation site within the oxide before it is able to recombine, leaving behind a net positive charge. The accumulation of this charge over time gives rise to a flat-band shift which can affect CIC and CTE. Traps are also generated at the silicon-silicon dioxide interface which can increase the component of surface dark signal. For operation in IMO, planned for the CGI detectors, these additional traps remain suppressed and so the net effect on dark signal is expected to be small. Flat-band shifts can also typically be mitigated through appropriate adjustment to the operating biases in-flight.

The degree of ionising damage has also been shown to be dependent on whether the detector is biased during the time it is irradiated. During operation the gates are biased during clocking which gives rise to an electric field within the dielectric layers. A carrier pair generated by an incident particle in the presence of this field therefore experiences forces in opposing directions, reducing the possibility for recombination. The best estimate of ionising damage is given by irradiating the device while biased and clocking, since this is what is routinely experienced in-flight. The estimated Total Ionising Dose (TID) for the CGI is expected to be reduced to a maximum of 2 krad through the inclusion of a glass window.[3] The effects of ionising damage are therefore not expected to be significant compared to other radiation damage effects.

The remaining fraction of energy loss is through displacement damage, whereby the proton interacts with a lattice site and displaces it from its original location to create a vacancy interstitial pair (Frenkel pair). Damage introduced through this mechanism is termed Non-Ionising Energy Loss (NIEL). The vast majority ($\geq$90%) of vacancy-interstitial pairs recombine shortly after production, however the remainder migrate through the lattice until they form stable defects.[10] These defects can have energy levels within the bandgap and so give rise to an increase in bulk dark current, including the formation of dark defects/hot pixels. Defects within the band-gap can also act to trap and defer signal charge to subsequent pixels and increase the total noise of the detector system. It is often the case that these trapping sites become the limiting factor for the performance of CCD based instruments in radiation environments, since the signal charge typically has to be transferred thousands of times before voltage conversion at the output. For the WFIRST CGI, the low expected signal levels mean the effect of bulk trapping sites must be understood to high precision since the loss of a single electron to a trapping site may represent the loss of the entire signal packet.

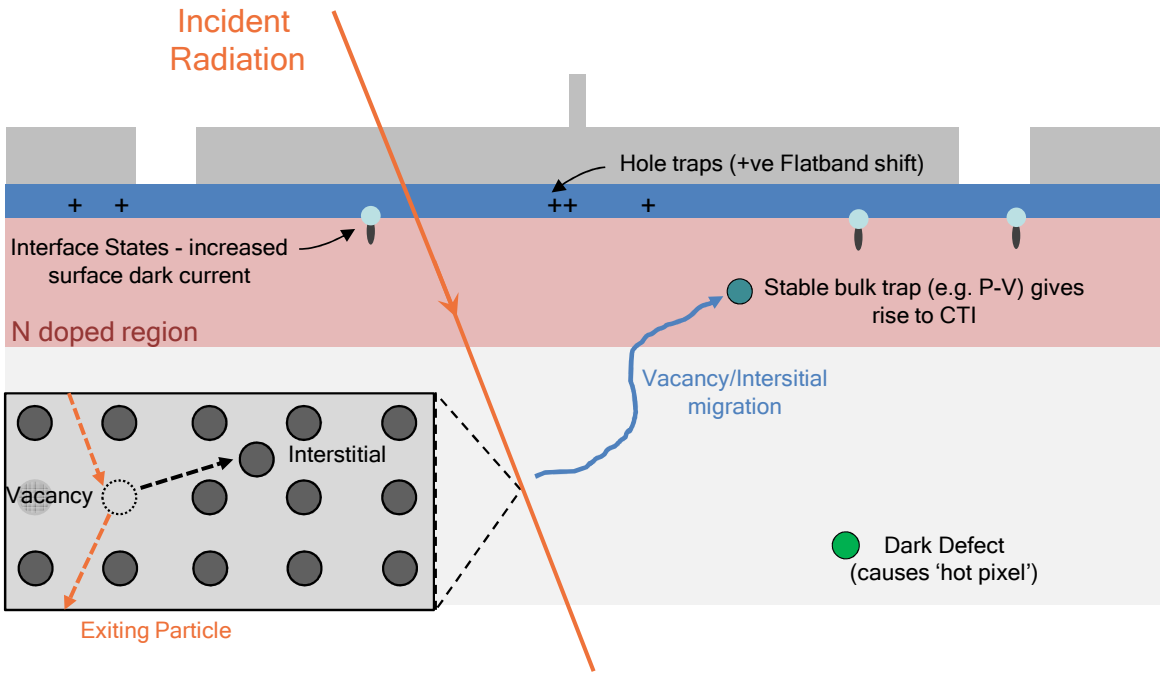

Figure 3: Illustration of primary radiation damage mechanisms for CCD (and hence EMCCD) technology. Figure adapted from Hall et al. (2014).[12]

The properties of charge trapping sites vary according to their composition. Different impurities and lattice complexes give rise to different energy levels with respect to the conduction band which is linked to variable times for both capture and emission. For CCDs, at least 5 different defect species have presently been identified that can contribute to CTI (Table 1). More information concerning how these defects influence performance can be found in Hall et al. (2014),[13] Murray et al. (2012)[14] and the contained references. As an overview, the impact of a particular defect species on the net CTI depends upon many factors, including:

1. The relative abundance of each defect species. Each defect has a different introduction rate, with the Si-E centre having approximately 10× the introduction rate of the VV^{--}, for example.[15]
2. The operating temperature. The probability that trapped charge will be emitted is strongly temperature dependant and so this affects the fraction of captured charge that can re-join the original signal packet before it is transferred onwards.
3. The operating speed (parallel and serial). This also affects the probability that the captured signal can re-join the original signal packet. The frame integration time can also affect the proportion of filled/unfilled traps between successive frames.
4. The optical scene during operation (including the presence of any diffuse optical background). This will influence the proportion of filled/unfilled traps that can affect the signal packet.

Since performance in a radiation environment is intrinsically linked to the population of stable trapping sites in the device, it follows that the best estimate of EOL performance will be derived from a device that has the same distribution of silicon defects as expected in-flight. As well as having variable time-scales for charge capture and emission, each defect and associated impurity has temperature dependant mobility and annealing characteristics.

The temperature at which the detector is irradiated can therefore have a profound impact on the final defect landscape within the silicon.[16] The best estimate of EOL performance will therefore be derived from a device that has been irradiated at the nominal mission operating temperature as opposed to room temperature, since in principle this will result in the same relative proportions of trapping sites that would be expected in-flight.

Table 1: Summary of literature values of known silicon defects in N channel CCDs.[13] Note that the emission cross sections are not well constrained and quoted values can vary by up to an order of magnitude. The emission time constant at 165 K (The operating temperature used for testing in this study) is also shown.

Trap species	Energy level below the conduction band (eV)	Emission cross section (cm^2)	Emission time constant (s) (165 K)
Si-E	0.46	5×10^{-15}	115
VV^-	0.39	2×10^{-15}	2.093
Unknown	0.30	5×10^{-16}	0.015
VV^{--}	0.21	5×10^{-16}	2.66×10^{-5}
Si-A	0.17	1×10^{-14}	7.98×10^{-8}

5. CRYOGENIC IRRADIATIONS

It has long been understood that the temperature at which silicon is irradiated can have a profound impact on the final distribution of stable defects within the lattice.[16] Since CTI performance following irradiation is intricately linked to the relative populations of different species of stable defects, the temperature at which the irradiation is performed can potentially have a profound effect on final performance values. Despite this, the majority of EOL performance estimates for CCD and CMOS image sensors to date are based upon the results from room temperature irradiations. The continued demand for increased sensitivity from silicon based image sensors places increased demand on detector performance throughout the mission lifetime. In such situations, cryogenic irradiations may become increasingly desirable since the discrepancy in performance following cryogenic irradiation and the room temperature equivalent can greatly impact the predicted achievable science of the mission.

The first documented cryogenic irradiation for a CCD based instrument was performed in 2003 and focused on the annealing behaviour of hot-pixel defects in the Hubble WFC-3 detectors.[17] A key conclusion was that there existed a population of hot-pixel defects that annealed following a room temperature anneal and a population that remained stable. The study was influential in highlighting how the relative concentration of defects within the device can be expected to vary according to the temperature at which the irradiation is performed. Additional investigations performed since this study have also presented findings that are consistent with this conclusion. A study performed by Gow et al. (2015)[18] included the irradiation of a Swept Charge Device (SCD) at 238 K, where performance was seen to vary depending upon the subsequent room temperature anneal period. Also of note are the investigations performed by Hopkinson that entailed irradiation of CCD sensors that were flown on ESAs GAIA satellite[19] and also the investigations performed by Bautz et al. (2005) for the Chandra X-ray observatory.[20]

An agreed conclusion of each study is that the performance of the device following cryogenic irradiation changes following a room temperature anneal period. For the cases where a direct comparison between room temperature and cryogenic case is possible, the cryogenic performance was seen to measurably differ. These differences between the room temperature and cryogenic case support the broad conclusion that the population of defects and impurities that are mobile at the irradiation temperature will impact the final defect landscape. The changes following a room temperature anneal can potentially be explained through defects that were previously immobile becoming mobile, leading to a change in dark signal and CTI (Figure 4). Although these conclusions appear well founded, the exact mechanisms and trapping species responsible for measured differences are not

well understood. Consequently, the results from one investigation cannot be used to estimate those for another with different operating conditions.

Estimating the performance of the CCD201-20 following an expected WFIRST EOL fluence therefore required a separate investigation whereby a device was irradiated under operating conditions that were representative of what the CGI will experience in-flight. The results from post-irradiation characterisation could then be used to give an accurate estimation of EOL performance since the population of stable defects generated would be represent the in-flight case.

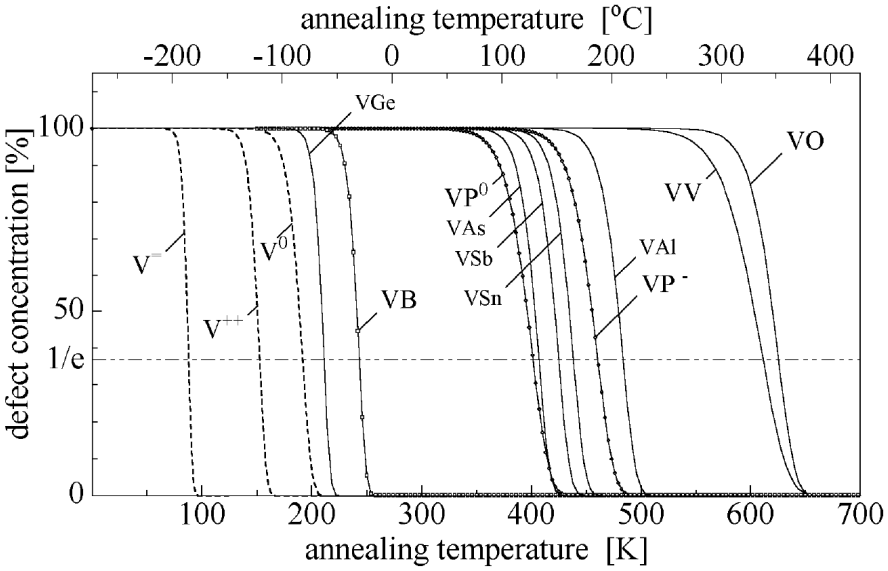

Figure 4: Schematic representation of vacancy and vacancy-defect pair annealing in silicon, based on literary values circa 1970-1990.[21] It should be noted that information on the annealing temperature of defects is dependent on many parameters and so this plot cannot be directly applied to a standard CCD without more detailed consideration. Despite this, it can be seen that a number of defects that are mobile at room temperature (≈300 K) are not mobile at the nominal operating temperature of the CGI (165 K). The population of trapping species and hence EOL performance is likely best estimated by irradiation at the nominal operating temperature as opposed to the room temperature equivalent.

6. WFIRST CGI CRYOGENIC IRRADIATION CAMPAIGN

Irradiation under cryogenic conditions places numerous constraints on the equipment and test methods that are possible following post-irradiation characterisation. The need to both irradiate and characterise at cryogenic temperatures requires the system to be permanently under vacuum and at a stable temperature until testing has completed. A cryogenic irradiation test system was designed with these points in mind and allowed the device to be repeatedly irradiated and characterised while maintaining the sensor at the nominal operating temperature of 165 K.[18]

A total of 4 separate irradiations were performed (Table 2) on a single science grade CCD201-20 at the Synergy Health Helios-3 beamline, Harwell, U.K (Figure 5). The primary proton beam energy was 5 MeV and so fluences were normalised to the 10 MeV equivalent fluence (Table 2). The device was unshielded for each irradiation however aluminium shielding was present within the cryostat to protect proximity electronics from damage (Figure 5). Each irradiation was performed with the detector biased and clocking in order to replicate flight conditions as accurately as possible.

A 7-day gap seperated successive fluences during which the post-irradiation characterisation was performed. Previous investigations had demonstrated that a degree of isothermal annealing can be expected following irradiation that takes a measurable amount of time to settle.[22] A two-day isothermal anneal took place following each irradiation whereby the device was allowed to settle to a stable state before post-irradiation characterisation took place. Measurements of annealing through "trap pumping"[14] and dark signal showed that the vast majority of annealing had completed by this time.

Temperature was controlled and monitored monitored through use of multiple platinum resistance temperature sensors attached to both the cooling system and ceramic package of the CCD201-20. The sensors were coupled to a temperature controller and resistive heater to allow automated temperature control. The maximum temperature variability across the entire 6-week campaign was measured as ± 2 K and typically occurred over a short period as the system thermally coupled to the proton beamline immediately prior to an irradiation. During post-irradiation characterisation, a much higher temperature stability of ± 0.1 K was routinely achieved. This minimised the risk of any unwanted thermal annealing between successive irradiations.

The detector was operated at a horizontal scan rate of 700 kHz, with a parallel clock delay of approximately 6μs, such that the time taken to transfer from row to row was approximately 12μs. The device was operated at standard e2v datasheet values[4] with the exception of the ϕDC and $R\phi$2HV biases which were adjusted to 4.3 V and 40.9 V respectively, resulting in a multiplication gain value of $\approx$154. The nominal frame integration time for CTI measurements was 100 s and the sensor was powered and maintained at 165 K throughout the entire campaign. These operating parameters were consistent with those used in a previous room temperature irradiation investigation, described in detail within Harding et al. (2015)[3] and Bush et al. (2015).[23] The use of consistent operating conditions and test methods allowed as fair a comparison as possible between the room temperature and cryogenic irradiation case.

Measurements of CTI and dark signal following the final fluence indicated little/no performance degradation and subsequent investigation highlighted that a negligible amount of displacement damage was delivered during this irradiation. The final cumulative fluence of the device was therefore estimated to be of order 5.25×10^9 protons/cm^2, which is within the error on dosimetry for the penultimate cumulative fluence.

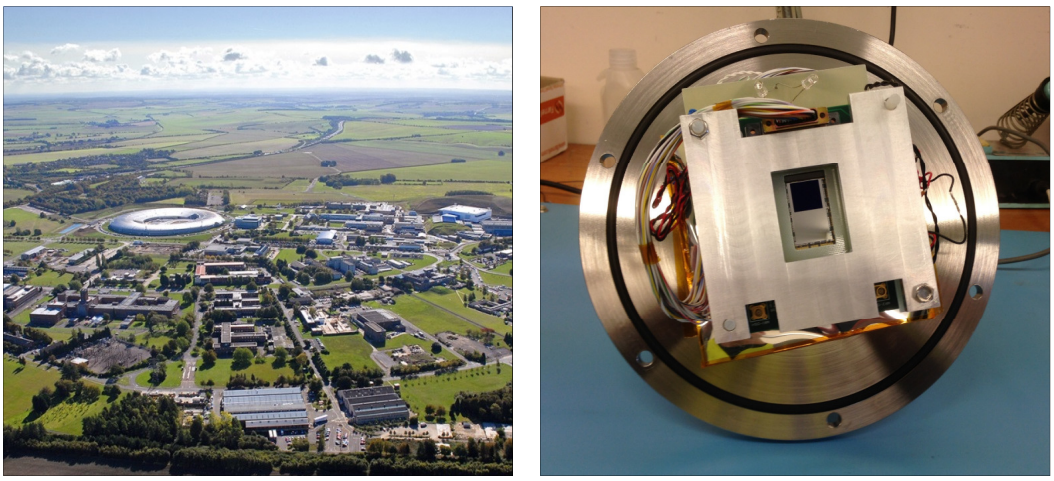

Figure 5: Left: Harwell Campus, U.K. Right: CCD201-20 mounted to camera head with shielding in place for proximity electronics.

Table 2: Proton fluences delivered to the CCD201-20 in the cryogenic irradiation campaign. Dosimetry was performed by staff at the irradiation facility and is quoted to be accurate to within 10%. Measurements following the final fluence indicated little/no performance degradation and subsequent investigation highlighted that a negligible amount of displacement damage was delivered during this irradiation. The final cumulative fluence of the device was therefore estimated to be of order 5.25×10^9 protons/cm^2, which is within the error on dosimetry for the penultimate cumulative fluence. The cumulative TID was estimated using the NIST PSTAR stopping tables for energy deposition of a 5 MeV proton beam into silicon dioxide.[24] 10 MeV equivalent fluences were calculated using the Non-Ionising Energy Loss normalisation function, described in detail Burke,[25] Van Lint[26] and in CCDs by Srour et al.[27]

Relative time of irradiation	5 MeV proton fluence (protons/cm^2)	10 MeV cumulative proton fluence (protons/cm^2)	Estimated cumulative TID (krad)
t_0	5.39×10^8	1.0×10^9	0.52
t_0 + 1 week	8.04×10^8	2.5×10^9	1.31
t_0 + 2 weeks	1.34×10^9	5.0×10^9	2.36
t_0 + 3 weeks	1.34×10^9	7.5×10^9	3.93

7. POST IRRADIATION CHARACTERISATION RESULTS

Following each irradiation and the subsequent anneal wait period the device was tested for performance parameters deemed most critical to the CGI, including low signal CTI, parallel CIC and thermal dark signal. The initial results for each of these metrics are discussed here, however a more detailed analysis, including other performance parameters and the impact of room temperature annealing on CTI, will be included in a future publication.

7.1 Thermal Dark Signal

Thermal dark signal was measured by taking multiple frames at long integration times (nominally 1, 2 and 4 hours) following each irradiation. Cosmic ray events were discounted through the comparison of images and removal of signals above a fixed threshold that were unique to a given frame. A linear fit to the accumulated signal as a function of integration time allowed calculation of the generation rate in units of e$^-$/pix/s. An expected linear increase in dark signal was observed as a function of cumulative fluence (Figure 6). This trend has been observed in other studies and is consistent with expectations.[10] Comparison to the results of room temperature irradiation described in Bush et al (2015) highlight a higher factor increase for an equivalent proton fluence when compared to the room temperature case.[23] Following a one week room temperature anneal period dark current was observed to return to what may be expected for a room temperature equivalent dose, measured as $(1.14\pm0.10)\times10^{-4}$ e$^-$/pix/s for an estimated 5.25×10^9 10 MeV proton fluence. An observed decrease in dark signal following a room temperature anneal is consistent with that observed in Gow et al (2015).[18]

The device was operated in IMO throughout the campaign and so the dominant contribution to the measured dark signal would have been from defects generated within the silicon bulk. Mid-band defects are responsible for the majority of bulk dark signal contribution,[10] and so the measurement of higher dark signal at cryogenic temperatures indicates a higher density of such defects are present following irradiation at 165 K when compared to the 298 K case. The significant reduction in bulk dark signal following the room temperature anneal period also indicates that a proportion of the defects responsible anneal within the temperature range of 165 K to 298 K. One such candidate is the substitutional Boron-Vacancy complex (BV), which has a measured donor energy level of 0.37 eV and a characteristic anneal temperature of approximately 260 K[21,].[16]

An interesting observation is the correlation of this postulation with the findings of Gow et al. (2015)[18] whereby the proton irradiation of a Swept Charge Device (SCD) at $\approx$ 238 K showed a significant dark current anneal (77%) following a 12 day room temperature anneal. The irradiation performed in this investigation was

also performed above the characteristic anneal temperature of the BV complex and the measured dark signal was also observed to decrease significantly following the room temperature anneal period. The importance of the BV complex to these observations remains speculative at this point, however serves as an example of how the irradiation temperature can significantly impact certain performance attributes through the presence or absence of certain stable defects.

The baselined WFIRST CGI dark current requirement is 5×10^{-4} e^-/pix/s based upon models of typical observation targets and single frame observation times in the range 100 to 300 s.[3] The measured dark current reaches this threshold at a cumulative fluence of 2.5 $\times10^{-9}$ protons cm^{-2}. Realistic expected cumulative fluences are expected to be of this level or below, depending upon the chosen shielding, hence these findings are positive with respect to the mission. Use of a room temperature anneal allows the detector to remain below the threshold value even at the higher fluence levels.

7.2 X-ray CTI

The signals that the CGI will routinely image are expected to be around the single electron level, and so the results of X-ray CTI alone are not indicative of true expected mission performance. However, useful information can be concluded from the measurement that gives further insight into the differences between the room temperature and cryogenic irradiation cases. Ultimately, this information can be used to optimise the devices for CTI at all signal levels, making this measurement important with respect to the long-term goal of optimising the CCD201-20 for best possible science performance.

X-ray CTI was measured through use of a fixed Fe^{55} with an activity of approximately 48 kBq placed approximately 20 cm from the detector. The frame integration time was 100 s, typical of what the CGI detectors are baselined to experience, giving rise to an X-ray density of one event ≈2700 pixels. These operating conditions are consistent with those of the investigation described in Bush et al. (2015).[23] The CTI value was measured following each irradiation through measurement of the remaining X-ray signal as a function of row or column position for serial and parallel X-ray CTI respectively. A linear fit to this data allowed calculation of the signal lost per transfer, which when expressed as a fraction of the total input signal ($\approx 1616e^-$) gave a value for the CTI.

The increase in CTI was found to be approximately linear as a function of the total cumulative fluence (Figure 7), exhibiting a trend observed in other studies.[28] When these findings are compared to the results of the room temperature irradiation, significantly higher CTI is observed for the same cumulative fluence level; an approximate factor $\times4$ increase for both parallel and serial CTI for the cryogenic case compared to the room temperature case depending upon the device under comparison.[23] This finding strongly suggests that the relative populations of defects following the cryogenic irradiation is different to that of the room temperature case. This information alone, however, is insufficient to distinguish the exact differences in the defect landscape between the two cases. The X-ray CTI measurement probes the charge capture process and so all trapping sites that empty between successive frames contribute to the net CTI measurement. While no defect specific information can be discerned, the observation of such a large difference between each investigation is an important, useful conclusion.

7.3 Parallel Clock Induced Charge (CIC)

An increase in parallel CIC was measured following each successive fluence however this was not believed to be due to the effects of displacement damage. The irradiations were all performed with the detector biased and clocking which in turn exacerbates the effect of the ionising component of the proton beam.[10] The ionising component would have given rise to a small yet measurable flat-band shift within the CCD pixels. Since CIC is exponentially dependant on the clock amplitude, this would have given rise to an increase in CIC as a function of cumulative fluence.

The increase in CIC was measured to be approximately 30% following a TID of approximately 2.36 krad for IMO operation at datasheet operating voltages and the clock frequencies used for this study (Table 3). The CIC requirement for each of the CGI imaging sensors has been achieved in the studies described within Harding et al. (2015)[3] for the CCD201-20 and so the observed increase is not a major concern. Typically, the effects of flat-band shifts can be mitigated through appropriate adjustment of clock amplitudes in-flight. The total shift

will depend on the accumulated TID throughout the mission, which for the CGI is expected to be reduced to a maximum of 2 krad through the inclusion of a glass window.[3] This limit is lower than the final estimated TID delivered in this study.

We note that serial CIC has not been measured within this investigation, and is an important contributor to the total combined spurious noise. However, the effect of radiation damage under biased cryogenic conditions has been demonstrated through the measurement of the effects on parallel CIC alone. Since the physical mechanisms for CIC generation remain consistent between each component, this information remains useful as a demonstration of what to expect from the total CIC contribution in-flight.

7.4 Low signal CTI (EPER and FPR)

CTI was measured at signal levels of $\approx 10e^-$ using the Extended Pixel Edge Response (EPER) technique whereby multiple frames of illumination were obtained with appropriate parallel and serial overscan to measure charge tails due to the capture and subsequent release of signal by trapping sites. The EPER technique probes the trap emission process and will typically only account for defects with emission time constants comparable to the column or row readout time for serial and parallel CTI respectively. Measurement of low signal parallel CTI was also performed using the First Pixel Response (FPR) method which probes the charge capture process for all relevant defects that have released their charge between successive frames.

FPR and EPER at low signal levels are applicable measurements for estimating CTI for the case of the visible imager, since this will image low intensity PSFs from the target planet. The leading edge of this PSF will be diminished to the effect of charge capture (estimated by FPR), and a fraction of this charge will be then be emitted giving rise to a tail that follows the PSF (EPER result). Each measurement combined is therefore useful in determining the degree of distortion that may occur as a function of total accumulated dose. For the case of the IFS, the signal is spectrally dispersed across the entire image area of the detector into a series of lenslet images.[3] In this instance, the effect of CTI will be to perturb the position of a lenslet image within the array which may cause distortion in the recorded spectra from planetary atmospheres. Once again, the information for low signal EPER and FPR can be used to quantify this effect and estimate the maximum permissible distortion.

For the EPER measurements the CTI increase was observed to be linear with respect to the cumulative fluence (Table 3). Once again, higher CTI was measured for the cryogenic case when compared to the room temperature investigation.[23] Parallel EPER CTI was measured to be $(3.94\pm0.45)\times10^{-4}$ for a fluence of 2.5×10^9protons/cm^2 delivered at room temperature compared to $(8.31\pm0.52)\times10^{-4}$ for the cryogenic case, an approximate factor 2 difference. The operating conditions used in each investigation were consistent and so the difference is once again most likely due to a disparity in the defect landscape present following a room temperature irradiation when compared to the cryogenic case. It is interesting to note the factor difference for EPER is lower than that measured for X-ray CTI in this study.

A linear relationship with cumulative fluence was also observed using the FPR technique (Figure 8). No measurement of FPR was performed during the room temperature irradiation investigation and so a direct comparison is not possible. However, the relevant processes for this measurement are similar to those probed using X-ray CTI, albeit at a smaller signal level. Thus, it is likely the case that the FPR CTI result under cryogenic conditions would be worse than that for the room temperature case.

Table 3: Summary of results from pre- and post-irradiation testing of each device. Results from the final cumulative proton fluence (7.5×10^9 protons/cm^2) are not included since it was later discovered this fluence was unsuccessful.

	10 MeV Cumulative Proton Fluence (protons/cm^2)			
Parameter	Pre-Irradiation	$(1.01\pm0.10)\times10^9$	$(2.52\pm0.18)\times10^9$	$(5.04\pm0.31)\times10^9$
Image Area Dark Signal (e$^-$/pixel/s)	$(4.89\pm0.42)\times10^{-5}$	$(2.01\pm0.13)\times10^{-4}$	$(5.01\pm0.48)\times10^{-4}$	$(8.06\pm0.52)\times10^{-4}$
Parallel CIC$^{(i)}$ (e$^-$/pixel/frame)	$(4.38\pm0.15)\times10^{-2}$	$(4.56\pm0.13)\times10^{-2}$	$(4.85\pm0.12)\times10^{-2}$	$(5.50\pm0.30)\times10^{-2}$
Fe^{55} Parallel CTI$^{(ii)}$	$(0.569\pm1.0)\times10^{-6}$	$(2.76\pm0.13)\times10^{-5}$	$(1.31\pm0.05)\times10^{-4}$	$(3.18\pm0.18)\times10^{-4}$
Fe^{55} Serial CTI$^{(ii)}$	$(1.67\pm2.08)\times10^{-6}$	$(8.63\pm2.32)\times10^{-6}$	$(4.12\pm0.35)\times10^{-5}$	$(1.03\pm0.08)\times10^{-4}$
FPR Parallel CTI: (signal $\approx 10e^-$)	$(3.79\pm5.45)\times10^{-6}$	$(1.66\pm0.07)\times10^{-4}$	$(4.08\pm0.08)\times10^{-4}$	$(7.06\pm0.29)\times10^{-4}$
EPER Parallel CTI$^{(iii)}$: (signal $\approx 10e^-$)	$(8.88\pm0.49)\times10^{-5}$	$(3.46\pm0.16)\times10^{-4}$	$(8.31\pm0.52)\times10^{-4}$	$(2.33\pm0.11)\times10^{-3}$
EPER Serial CTI$^{(iii)}$: (signal $\approx 10e^-$)	$(1.65\pm0.47)\times10^{-5}$	$(1.50\pm0.10)\times10^{-4}$	$(6.84\pm0.15)\times10^{-4}$	$(1.59\pm0.03)\times10^{-3}$

$^{(i)}$ Measured at datasheet voltages[4]

$^{(ii)}$ X-ray CTI measured using an integration time of 100s with an X-ray density of $\approx$ 1 X-ray per 2700 pixels.

$^{(iii)}$ EPER CTI measured using a full-frame of illumination, an integration time of 100s and integrating the total signal within serial/parallel charge tails

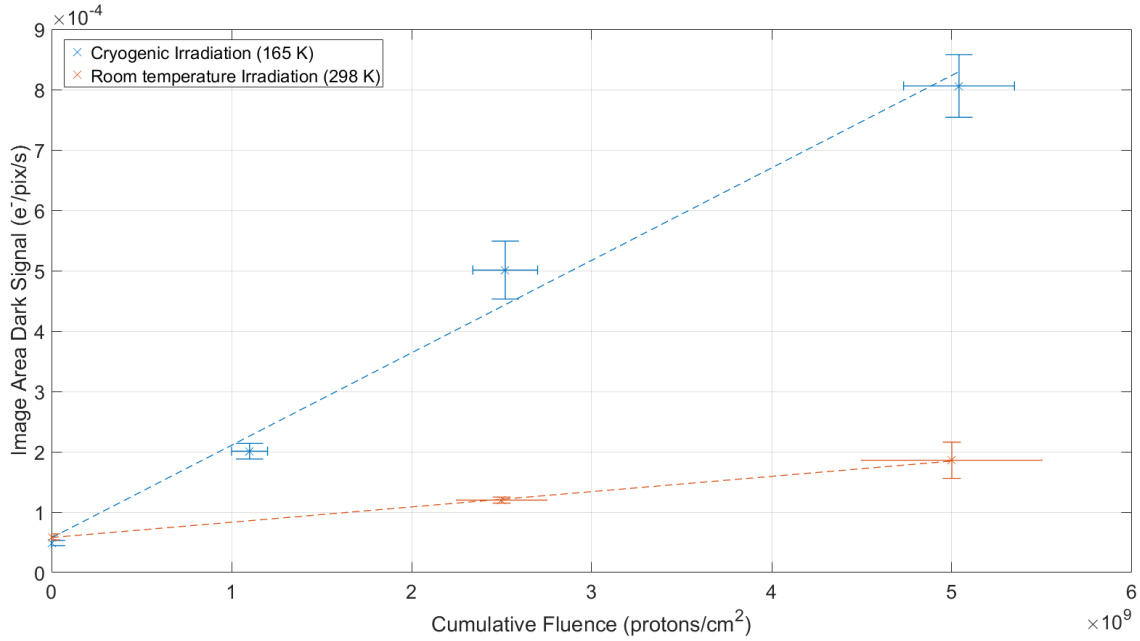

Figure 6: Image area dark signal as a function of cumulative proton fluence. Results are shown for the cryogenic irradiation campaign described in this study (Table 3) and from the previous room temperature irradiation[23]). A result from an additional room temperature irradiation on a CCD201-20 tested under the same conditions is also shown that will be discussed in more detail within a future publication.

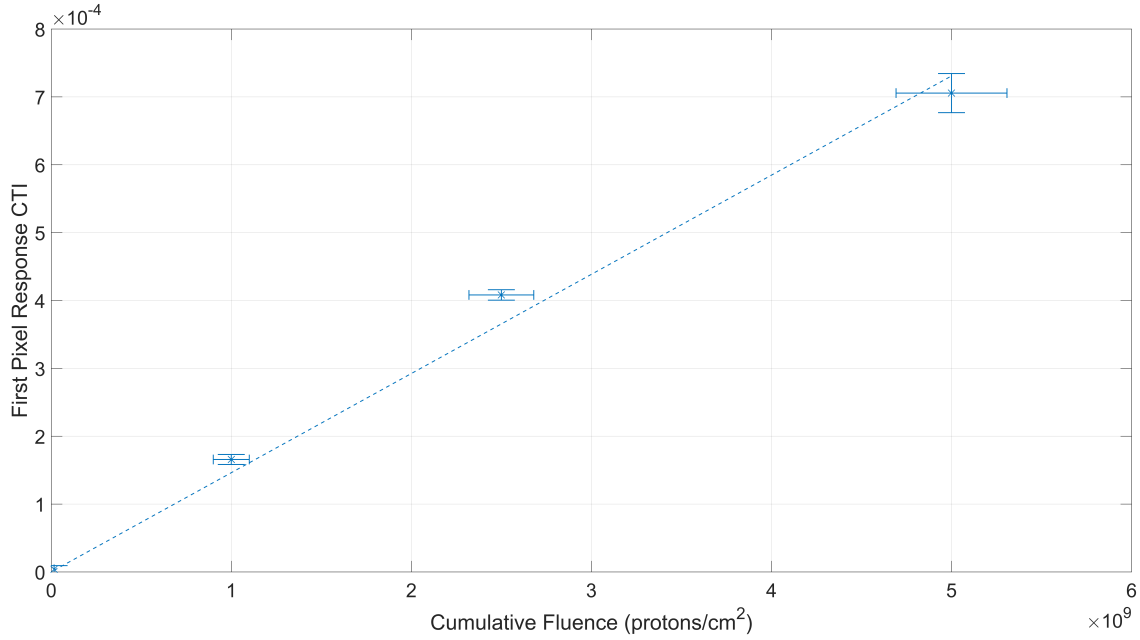

Figure 8: CTI measured using the First Pixel Response method as a function of cumulative proton fluence (Table 3).

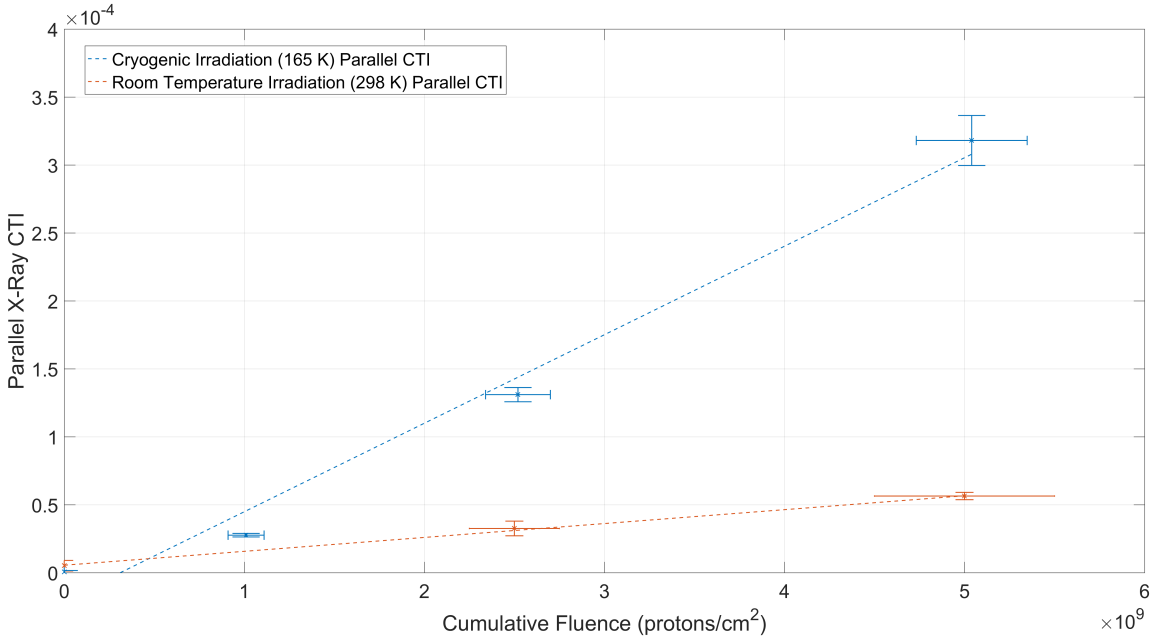

Figure 7: Parallel X-ray CTI as a function of cumulative proton fluence. X-ray CTI was measured using an integration time of 100 s and an X-ray density of 1 per ≈2700 pixels. Results are shown for the cryogenic irradiation campaign described in this study (Table 3) and from the previous room temperature irradiation[23]). A result from an additional room temperature irradiation on a CCD201-20 tested under the same conditions is also shown that will be discussed in more detail within a future publication.

8. CONCLUSIONS AND FUTURE WORK

A key conclusion is that, for the operating conditions of this study, irradiation under biased, cryogenic conditions gives rise to significantly higher performance degradation for a given fluence when compared to the room temperature equivalent. For each of the results discussed here, the differences can be explained through a difference in the landscape of silicon defects between the cryogenic and room temperature case. When one is reminded that missions typically incorporate a radiation design factor of ×2 to account for possible variations in expected fluence, the benefit of using cryogenic irradiations to estimate performance becomes immediately apparent.

The results for the effect of radiation damage on the CCD201-20 with respect to the WFIRST CGI remain promising. The increase in dark current and possible increase in CIC (dependant in TID) are both manageable. CTI degradation remains the focus point for future study and work is under way to quantify the maximum tolerable CTI for each of the coronagraph sensors. Techniques are being developed and implemented that can probe the landscape of silicon defects within the CCD201-20 to a very high level of precision. The technique of 'trap pumping' has been used successfully in previous studies to provide the spatial location and properties of individual silicon defects.[29,14,12] The technique has been developed further to be applicable for the case of the CCD201-20 so that the densities and properties of defects most applicable for performance of the coronagraph can be accurately measured. Knowledge of the relative abundance of different trapping species will inform device optimisation strategies in the laboratory with the aim of providing the best performance for the IFS and visible imager in the presence of radiation induced damage.

9. ACKNOWLEDGEMENTS

This work was carried out by the Center for Electronic Imaging and the Jet Propulsion Laboratory, California Institute of Technology, under a contract with the National Aeronautics and Space Administration.

REFERENCES

[1] Spergel, D., Gehrels, N., and et al., B., "Wide-Field InfrarRed Survey Telescope-Astrophysics Focused Telescope Assets WFIRST-AFTA 2015 Report," *ArXiv e-prints* (Mar. 2015).

[2] Noecker, M. C., Zhao, F., Demers, R., Trauger, J., Guyon, O., and Jeremy Kasdin, N., "Coronagraph instrument for WFIRST-AFTA," *Journal of Astronomical Telescopes, Instruments, and Systems* **2**(1), 011001 (2016).

[3] Harding, L. K., Demers, R. T., Hoenk, M., Peddada, P., Nemati, B., Cherng, M., Michaels, D., Neat, L. S., Loc, A., Bush, N., Hall, D., Murray, N., Gow, J., Burgon, R., Holland, A., Reinheimer, A., Jorden, P. R., and Jordan, D., "Technology advancement of the CCD201-20 EMCCD for the WFIRST coronagraph instrument: sensor characterization and radiation damage," *Journal of Astronomical Telescopes, Instruments, and Systems* **2**, 011007 (Jan. 2016).

[4] e2v technologies, "e2v ccd201-20 datasheet,"

[5] Jerram, P., Pool, P. J., Bell, R., and Burt, D. J. e. a., "The llccd: low-light imaging without the need for an intensifier," *Proc. SPIE* **4306**, 178–186 (2001).

[6] Robbins, M. S. and Hadwen, B. J., "The noise performance of electron multiplying charge-coupled devices," *Electron Devices, IEEE Transactions on* **50**(5), 1227–1232 (2003).

[7] Basden, A. G., Haniff, C. A., and Mackay, C. D., "Photon counting strategies with low-light-level CCDs," **345**, 985–991 (Nov. 2003).

[8] e2v technologies, "Low-light technical note 4 dark signal and clock-induced charge in l3visiontm ccd sensors," *JATIS* (July 2015).

[9] Daigle, O., Gach, J.-L., Guillaume, C., Lessard, S., Carignan, C., and Blais-Ouellette, S., "CCCP: a CCD controller for counting photons," in [*Society of Photo-Optical Instrumentation Engineers (SPIE) Conference Series*], *Society of Photo-Optical Instrumentation Engineers (SPIE) Conference Series* **7014**, 6 (July 2008).

[10] Hopkinson, G. R., Dale, C. J., and Marshall, P. W., "Proton effects in charge-coupled devices," *IEEE Transactions on Nuclear Science* **43**, 614–627 (Apr. 1996).

[11] Oldham, T. R., McLean, F. B., Jr, H. E. B., and McGarrity, J. M., "An overview of radiation-induced interface traps in MOS structures," *Semiconductor Science and Technology* **4**(12), 986 (1989).

[12] Hall, D. J., Murray, N. J., Holland, A. D., Gow, J., Clarke, A., and Burt, D., "Determination of in situ trap properties in ccds using a single-trap pumping technique," *Nuclear Science, IEEE Transactions on* **61**(4), 1826–1833 (2014).

[13] Hall, D. J., Murray, N. J., Gow, J. P. D., Wood, D., and Holland, A., "Studying defects in the silicon lattice using CCDs," *Journal of Instrumentation* **9**, C12004 (Dec. 2014).

[14] Murray, N., Holland, A., Gow, J., Hall, D., Tutt, J. H., Burt, D., and Endicott, J., "Mitigating radiation-induced charge transfer inefficiency in full-frame ccd applications by pumpingtraps," (2012).

[15] Seabroke, G., Holland, A., and Cropper, M., "Modelling radiation damage to ESA's Gaia satellite CCDs," in [*High Energy, Optical, and Infrared Detectors for Astronomy III*], **7021**, 70211P (July 2008).

[16] Watkins, G. D., "Intrinsic defects in silicon," *Materials Science in Semiconductor Processing* **3**(4), 227 – 235 (2000).

[17] Polidan, E. J., Waczynski, A., Marshall, P. W., Johnson, S. D., Marshall, C. J., Reed, R. A., Kimble, R. A., Delo, G., Schlossberg, D., Russell, A. M., Beck, T., Wen, Y., Yagelowich, J., Hill, R. J., and Wassell, E., "Hot pixel behavior in wfc3 ccd detectors irradiated under operational conditions," *Proc. SPIE* **5167**, 258–269 (2004).

[18] Gow, J. P. D., Smith, P. H., Pool, P., Hall, D. J., Holland, A. D., and Murray, N. J., "Proton irradiation of a swept charge device at cryogenic temperature and the subsequent annealing," *Journal of Instrumentation* **10**(01), C01037 (2015).

[19] Hopkinson, G. R., Gare, P., and Sarri, G., "Effects of Low Temperature Proton Irradiation on a Large Area CCD for Astrometric Applications," *IEEE Transactions on Nuclear Science* **57**, 2035–2043 (Aug. 2010).

[20] Bautz, M., Prigozhin, G., Kissel, S., Lamarr, B., Grant, C., and Brown, S., "Anomalous Annealing of a High-Resistivity CCD Irradiated at Low Temperature," *IEEE Transactions on Nuclear Science* **52**, 519–526 (Apr. 2005).

[21] Moll, M., "Radiation damage in silicon particle detectors. microscopic and macroscopic properties," *PhD Thesis, Hamburg University* (1999).

[22] "Assessment of space proton radiation-induced charge transfer inefficiency in the ccd204 for the euclid space observatory," *JINST* **7**(01), C01030 (2012).

[23] Bush, N., Hall, D., Holland, A., Burgon, R., Murray, N., Gow, J., Soman, M., Jordan, D., Demers, R., Harding, L., Hoenk, M., Michaels, D., Nemati, B., and Peddada, P., "The impact of radiation damage on photon counting with an EMCCD for the WFIRST-AFTA coronagraph," *Proc. SPIE* **9605**, 96050E–96050E–15 (2015).

[24] Berger, M. J., "ESTAR, PSTAR, ASTAR: A PC package for calculating stopping powers and ranges of electrons, protons and helium ions, version 2," tech. rep. (Dec. 1993).

[25] Burke, E. et al., "Energy dependence of proton-induced displacement damage in silicon," *Nuclear Science, IEEE Transactions on* **33**(6), 1276–1281 (1986).

[26] Van Lint, V. A., "The physics of radiation damage in particle detectors," *Nuclear Instruments and Methods in Physics Research Section A: Accelerators, Spectrometers, Detectors and Associated Equipment* **253**(3), 453–459 (1987).

[27] Srour, J., Marshall, C. J., and Marshall, P. W., "Review of displacement damage effects in silicon devices," *Nuclear Science, IEEE Transactions on* **50**(3), 653–670 (2003).

[28] Holland, A. D., Abbey, A. F., Lumb, D. H., and McCarthy, K. J., "Proton damage effects in EEV charge-coupled devices," *Proc. SPIE* **1344**, 378–395 (1990).

[29] Murray, N. J., Burt, D. J., Hall, D., and Holland, A. D., "The relationship between pumped traps and signal loss in buried channel ccds," in [*SPIE Optical Engineering+ Applications*], 88600H–88600H, International Society for Optics and Photonics (2013).